The Proof-of-Concept for Raindrop Size Distribution Retrieval Using Combined Dual-frequency Radar DFR

Liang Feng [1], Jiefan Yang [1] , Zeyong Guo [3], Jiming Sun [2], Yue Sun [2], Huiling Yang [2] Xiangfeng Hu[4]

[1]State Key Laboratory of Atmospheric Environment and Extreme Meteorology, Institute of Atmospheric Physics, Chinese Academy of Sciences, Beijing 100029, China
[2]Laboratory of Cloud-Precipitation Physics and Severe Storms, Institute of Atmospheric Physics, Chinese Academy of Sciences, Beijing 100029, China
[3]Meteorological Administration Tornado Key Laboratory, Guangdong-Hong Kong-Macao Greater Bay Area Academy of Meteorological Research, Yangjiang 529500, China
[4]Weather Modification Office of Hebei Province, Shijiazhuang 050021, China

Correspondence to: Jiefan Yang (yjf@mail.iap.ac.cn), Zeyong Guo (guozeyong1982@163.com)

Abstract. Accurate retrieval of raindrop size distributions (DSDs) is essential for understanding cloud and precipitation microphysics. The dual-frequency ratio (DFR) measured by dual-frequency radars is independent of the normalized intercept parameter (Nw) and depends solely on the mass-weighted mean diameter (Dm). This characteristic makes DFR a powerful parameter for DSD retrieval. However, the DFR-Dm relationship is subject to a dual-solution ambiguity, particularly for smaller particles. This study demonstrates that W-band reflectivities obtained through scattering simulations based on measured raindrop size distributions, combined with the DFR(Ka, W) constraint, effectively mitigate the DFR(X, Ka)-Dm dual-solution ambiguity. The results demonstrate that incorporating the DFR(Ka, W) constraint substantially reduces the DFR–Dm ambiguity, raising the proportion of data with a unique Dm solution from 35.38% (DFR(X, Ka) alone) to 87.5%. The proposed framework shows potential advantages over conventional approaches, particularly for weak echoes (< 20 dBZ), where conventional methods fail but the proposed framework maintains robust accuracy. This proof-of-concept study provides a reference framework for future three-frequency radar DSD retrieval.

1 Introduction

As a fundamental parameter in cloud and precipitation microphysics, the raindrop size distribution (DSD) characterizes the size distribution of precipitation particles (Marshall and Palmer, 1948; Ulbrich, 1983; Testud et al., 2001). Accurate retrieval of DSD is crucial for advancing research in cloud and precipitation microphysics, developing and evaluating cloud microphysics schemes in numerical models, supporting weather modification activities, and understanding cloud–climate interactions (Liu et al., 2021). Consequently, how to accurately retrieve DSD has always been an important research topic in radar meteorology. However, due to the variability in precipitation particle shape, density, size, orientation, and spectral characteristics, accurately quantifying the microphysical properties of cloud and precipitation systems using single-frequency radar remains a significant challenge (Li et al., 2023).

Numerous studies have demonstrated that the dual-frequency radar could retrieve DSD more accurately with the Dual-Frequency Ratio (DFR) (Seto et al., 2013; Liao and Meneghini, 2019a; Kubota et al., 2020). This technique employs two distinct wavelengths: one is chosen such that Rayleigh scattering dominates for most precipitation-sized particles, while the other is sufficiently short to trigger Mie scattering in the presence of large hydrometeors (Liao and Meneghini, 2019b). Since Mie scattering is more sensitive to particle size, an increase in particle diameter amplifies the difference in scattering characteristics between the two frequencies, resulting in a noticeable increase in DFR. This makes DFR a key diagnostic parameter for characterizing the DSD.

Another important advantage of the DFR is its independence on the normalized intercept parameter (Nw) when retrieving the DSD. Under the normalized gamma size distribution assumption with a fixed shape factor (μ), DFR depends only on the mass-weighted mean diameter (Dm). Meneghini et al. (2022) demonstrated that the retrieved DSD closely matches in situ observations when μ is set to 3. Most studies on DFR-based DSD retrieval have focused on the dual-frequency Ku/Ka-band radar aboard the Global Precipitation Measurement (GPM) satellite (Hou et al., 2014; Liao et al., 2014; Skofronick-Jackson et al., 2017, 2018; Iguchi et al., 2021; Seto et al., 2021; Iguchi and Meneghini, 2022; Ladino-Rincon et al., 2025).

A great challenge in DFR-based DSD retrieval is the DFR–Dm dual-solution. For example, when DFR ≤ 0, a single DFR value corresponds to two Dm values (Meneghini et al., 1992, 1997; Mardiana et al., 2004; Liao and Meneghini, 2005; Rose and Chandrasekar, 2005). A commonly used approach is to select the large Dm value as the solution, which often introduces retrieval errors, particularly in light precipitation (Mardiana et al., 2004; Meneghini et al., 2022). Another method is to discard data with DFR ≤ 0 and only use data with DFR > 0 to retrieve Dm, which results in considerable data loss (Wang et al., 2020; Liu et al., 2020).

To address the DFR–Dm dual-solution, Liao and Meneghini (2019) proposed a generalized dual-frequency ratio, denoted as DFR* ($DFR^* = dBZ(f_1) - \gamma \cdot dBZ(f_2)$, where $\gamma \in [0, 1]$). Although DFR* successfully avoids the ambiguity inherent in the original DFR formulation, it is no longer a function solely of Dm and introduces a dependence on Nw. Iguchi and Meneghini (2022) further introduced a retrieval approach based on the differential form of the dual-frequency radar equation, investigating the stability of Dm retrievals with respect to variations in initial conditions. However, this method primarily mitigates the dual-solution under conditions of strong attenuation (i.e., intense precipitation). Meneghini et al. (2022) also noted that it is not always possible to identify the correct solution among multiple candidates although the DFR–Dm dual-solution can be addressed analytically. Given that the dual-solution in the DFR-Dm relationship has not been adequately resolved, the GPM currently employs the R-Dm relationship to retrieve Dm (Seto et al., 2021).

This paper is structured as follows: Section 2 introduces the theoretical background of the DFR-Dm relationship, the overall DSD retrieval strategy, and a step-by-step retrieval framework. Section 3 presents the preprocessing steps, including attenuation correction, sensitivity analysis, and the construction of the retrieval algorithm based on scattering simulation. Section 4 provides a comprehensive evaluation of the proposed framework using case studies, ground-based disdrometer validation, and an independent validation strategy. Section 5 discusses the limitations and practical applicability of the proposed framework. Finally, Section 6 summarizes the key findings and outlines directions for future research.

2 Overall retrieval strategy

2.1 Retrieval Framework

The overall retrieval framework of this study is built upon the synergy between dual-frequency radar observations and T-matrix scattering simulations. Figure 1 presents the schematic diagram of the retrieval system. Blue boxes denote the results from scattering simulations, and green boxes represent those derived from radar observation data. The framework integrates three fundamental components: (1) observation-based inputs, including X/Ka-band dual-frequency radar reflectivities and 2DVD-measured raindrop size distributions; (2) physics-based simulation, where T-matrix scattering calculations are employed to derive theoretical relationships between radar observables and DSD parameters; and (3) multi-constraint retrieval, which combines DFR(X, Ka) and DFR(Ka, W) to resolve the Dm ambiguity while using LWC-Z_{Ka} relationship for liquid water content estimation.

The core concept of this method is rooted in the physical principle that the DFR at distinct frequency pairs, specifically X/Ka and Ka/W bands, exhibits distinct responses to variations in Dm. This disparity arises from differences in their sensitivity to particle size and scattering regime. In the DFR(X, Ka)-Dm relationship, the dual-solution means a single DFR corresponds to two Dm values when DFR(X, Ka) ≤ 0. To resolve this ambiguity, DFR(Ka, W) is employed, which operates at higher frequencies and exhibits a significantly narrower ambiguity zone than DFR(X, Ka)-Dm.

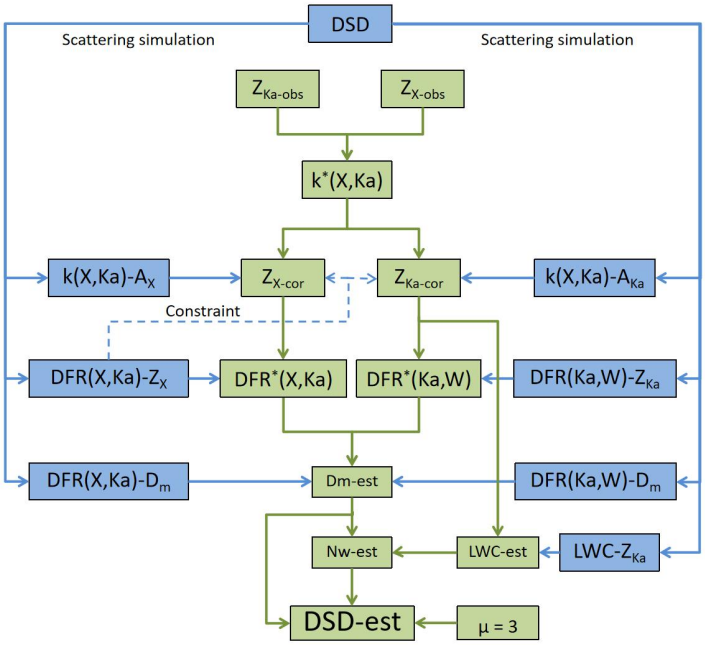

Figure 1. Flowchart of X/Ka dual-frequency radar retrieval for normalized gamma raindrop size distribution (Blue arrows indicate the scattering simulation workflow, while green arrows represent the retrieval workflow for real radar observation data).

2.2 Retrieval Procedure

The overall retrieval scheme and the detailed procedure is described as follows:

Step 1: The 2DVD observations of raindrop size distributions are collected as ground-truth measurements. According to the measuring principles of 2DVD, the number concentration of raindrops ($N(D_i)$: m^{-3} mm^{-1}) per unit volume per unit size interval at a discrete instant are calculated using the following equations:

$$N(D_i)_{2DVD}=\frac{1}{\Delta t\Delta D}\sum_{j=1}^{m_i}\frac{1}{A_jV_j} \tag{1}$$

where Δt is the time interval (60s is used in this study), i is the size index, j is the particle index, A_j (mm^2) and V_j($m\ s^{-1}$) are the sensing area and fall velocity for drop j, respectively; and m_i is the number of drops within size class i and time interval Δt. ΔD (mm) represents size-sorted categories of equivalent-volume diameters, and 0.2 mm is used.

The n-th moment of the DSD can be obtained by integrating the spectrum, as defined by Tokay and Beard (1996):

$$M_n=\int_{D_{min}}^{D_{max}} D^nN(D)dD \tag{2}$$

The subscripts min and max represent the minimum and maximum diameters of raindrops, respectively. The true values of Dm, liquid water content (LWC), and Nw can be derived from the moments of the DSD:

$$D_m=\frac{M_4}{M_3}=\frac{\int_{D_{min}}^{D_{max}} D^4N(D)_{2DVD}dD}{\int_{D_{min}}^{D_{max}} D^3N(D)_{2DVD}dD} \tag{3}$$

$$LWC=\frac{\pi}{6}M_3=\frac{\pi}{6}\times10^{-3}\int_0^{\infty} D^3N(D)_{2DVD}dD \tag{4}$$

$$Nw=\frac{4^4}{\pi\rho_w}\left(\frac{LWC}{D_m^4}\right) \tag{5}$$

where ρ_w is the density of water.

Step 2: T-matrix scattering calculations are performed to simulate radar reflectivities at X-, Ka-, and W-band frequencies (Z_X, Z_{Ka}, Z_W), specific attenuation at X-band and Ka-band (A_X, A_{Ka}), and differential specific attenuation [k(X, Ka)] based on the DSDs measured by 2DVD.

Step 3: The retrieval relationships of DFR(X, Ka)-Dm, DFR(Ka, W)-Dm, DFR(X, Ka)-Z_X, DFR(Ka, W)-Z_{Ka}, k(X, Ka)-A_X, k(X, Ka)-A_{Ka} and LWC-Z_{Ka} are established via fitting.

Step 4: Radar observed reflectivity of X-band and Ka-band ($Z_{X\text{-}obs}$, $Z_{Ka\text{-}obs}$) are input into the retrieval system and k^*(X, Ka) is calculated using $Z_{X\text{-}obs}$ and $Z_{Ka\text{-}obs}$. Using the retrieval relationships of k(X, Ka)-A_X and k(X, Ka)-A_{Ka}, A^*_X and A^*_{Ka} are obtained. The observed reflectivities $Z_{X\text{-}obs}$ and $Z_{Ka\text{-}obs}$ are finally corrected, yielding $Z_{X\text{-}cor}$ and $Z_{Ka\text{-}cor}$. Furthermore, the deviations exist in the reflectivity after correction when applying A^*_X and A^*_{Ka} to X- and Ka-band reflectivity. To address this issue, we impose constraints on the corrected reflectivity using the DFR(X, Ka)-Z_X relationship (see Section 3.3 for details).

Step 5: Based on the theoretical retrieval relationships for DFR(X, Ka)-Z_X and DFR(Ka, W)-Z_{Ka}, DFR*(X, Ka) and DFR*(Ka,W) corresponding to actual radar observations are retrieved from $Z_{X\text{-}cor}$ and $Z_{Ka\text{-}cor}$.

Step 6: Dm-est is retrieved using the combined DFR*(X, Ka) and DFR*(Ka, W) relationships, with the latter used to resolve ambiguity when DFR(X, Ka)$^* \leq 0$.

Step 7: LWC-est is retrieved from Ka-band reflectivity using the established LWC-Z_{Ka} relationship and Nw-est is computed from Dm-est and LWC-est using the DSD moment relationship.

Step 8: Dm-est and Nw-est are substituted into the normalized gamma distribution function (μ=3) to obtain the retrieved raindrop size distribution DSD-est. The normalized gamma distribution is as follow (Testud et al. 2001):

$$N(D)=N_W f(\mu)\left(\frac{D}{D_m}\right)^{\mu}\exp\left[\frac{-(4+\mu)D}{D_m}\right] \tag{6}$$

$$f(\mu)=\frac{6(4+\mu)^{\mu+4}}{4^4\Gamma(\mu+4)} \tag{7}$$

It should be emphasized that no fitting of the normalized gamma distribution to the measured DSD is involved in deriving the reference DSD parameters. The Dm, LWC, and Nw are computed directly from M_3 and M_4 via Eqs. (3)–(5), and are therefore independent of μ. The normalized gamma distribution (Eq. 6) with μ = 3 is used only at the final step of the retrieval (Step 8) to retrieve DSD from Dm-est and Nw-est.

3 Instrument and Data Processing

3.1 Instruments

The dataset utilized in this study comprises radar observations from an X/Ka dual-frequency radar and drop size distribution measurements from a 2-dimensional video disdrometer (2DVD). Both datasets were collected in vertical pointing mode at the meteorological observation site in Yangjiang, Guangdong Province, on May 1, May 11, June 11, 2022 and June 14, 2025. The X/Ka dual-frequency radar, developed by the 38th Research Institute of China Electronics Technology Group Corporation (CETC-38), employs a fully solid-state frequency-modulated continuous wave (FMCW) system with coaxial scanning and has undergone absolute calibration prior to field deployment. Its high temporal and spatial resolution enables the real-time tracking of precipitation system structural evolution. The 2DVD, developed by Austria's Joanneum Research, is designed to capture the two-dimensional size distribution and phase characteristics of precipitation particles. It provides essential ground-truth data for DSD research and phase identification algorithm validation. The main technical specifications of the X/Ka-band radar are presented in Table 1.

Table 1. Key specifications of X/Ka dual-frequency radar system

Paremeters	Specification
Operating Frequency	35.02 GHz(Ka-band) ; 9.37 GHz (X-band)
Antenna Diameter	1864 mm

Antenna Gain	54.6 dBi (Ka-band); 44.6 dBi (X-band)
Beamwidth	0.4° (Ka-band); 1° (X-band)
Range Resolution	≤ 30 m
Detection Capability	≤-38dBZ@10km(Ka-band); ≤-25dBZ@10km(X-band)
Measured Variables	Z, V, W, Z_{DR}, Φ_{DP}, K_{DP}, ρ_{HV}
Accuracy	Z ≤1.0 dBZ; V ≤ 1.0 m s^{-1}; W ≤ 1.0 m s^{-1}; Z_{DR} ≤ 0.2 dB; Φ_{DP} ≤ 1°; K_{DP} ≤ 0.2° km^{-1}; ρ_{HV} ≤ 0.01

As shown in Table 1, the mismatch in beamwidth between the X- and Ka-band leads to scale errors. The scale errors can be reduced by time averaging and spatial smoothing (Ellis and Vivekanandan, 2011). To mitigate the scale mismatch between the two frequencies, Ka-band reflectivities are temporally smoothed using a 3-point running mean. This increases the effective averaging scale along the time dimension, rendering the smoothed Ka-band sampling volume approximately equivalent to that of the X-band.

3.2 Scattering Simulation

The T-matrix method provides an efficient and rigorous approach for computing electromagnetic scattering by nonspherical particles, which was developed by Waterman (1965, 1971). By directly solving Maxwell equations with appropriate boundary conditions, the method is particularly suitable for modeling the scattering properties of axisymmetric hydrometeors, such as raindrops, snowflakes, and graupel. In this study, the T-matrix method is employed to simulate the scattering characteristics of measured raindrop size distributions at X-, Ka-, and W-band frequencies. The simulations serve as the theoretical foundation for developing a new DSD retrieval algorithm based on dual-frequency radar observations.

In the context of radar meteorology, the radar reflectivity is defined as follows (in units of $mm^6 \cdot m^{-3}$):

$$Z_{h,v}=\frac{\lambda^4}{\pi^5}\left|\frac{m^2+2}{m^2-1}\right|\int_{D_{min}}^{D_{max}}\sigma_{H,V}(D)N(D)dD \tag{8}$$

where λ is the wavelength of the electromagnetic wave, m is the complex refractive index of the precipitation particle, and $\sigma_{H,V}$ denotes the horizontal or vertical backscattering cross section. $Z_{h,v}$ represents the horizontal or vertical radar reflectivity. When expressed in terms of T-matrix elements, the Eq. 8 becomes:

$$Z_h=Cn_0\langle\sigma_H\rangle=2\pi Cn_0\langle\overline{M}_{11}-\overline{M}_{12}-\overline{M}_{21}+\overline{M}_{22}\rangle \tag{9}$$

$$Z_v=Cn_0\langle\sigma_V\rangle=2\pi Cn_0\langle\overline{M}_{11}+\overline{M}_{12}+\overline{M}_{21}+\overline{M}_{22}\rangle \tag{10}$$

where 〈 … 〉 denotes the volumetric ensemble average of the phase matrix elements for precipitation particles, and no represents the total number of particles per cubic meter. The constant C is defined as $C = 10^{18}\lambda^4/(\pi^5|K|^2)$, where K = (ε-1)/(ε+2), and ε is the dielectric constant of the hydrometeor, given by $\varepsilon=m^2$. These parameters are derived from the phase matrix outputs of T-matrix scattering simulations (Feng et al., 2019).

The axis-ratio model is still required in the T-matrix calculations because the scattering and extinction properties depend on particle shape. However, under vertically pointing observations, polarization-dependent differences are negligible and do not directly affect the retrieval framework. In this study, the raindrop axis ratio is determined using the following relationship (Tang et al., 2014):

$$r = 0.9971 + 0.2193D - 3.5105D^2 + 5.0746D^3 - 2.3559D^4 \tag{11}$$

Table 2. Complex refraction index of raindrops at X-, Ka-, and W-band at different temperatures.

Frequency/GHz	Temperature	Complex refraction index
X（9.37）	0℃	7.1421 - 2.8658*i
	10℃	7.6978 - 2.4756*i
	20℃	8.0227 - 2.0341*i
	30℃	8.1539 - 1.6212*i
Ka（33.44）	0℃	4.0271 - 2.4779*i
	10℃	4.5744 - 2.6973*i
	20℃	5.1486 - 2.8070*i
	30℃	5.7062 - 2.7885*i
W（93.75）	0℃	2.7370 - 1.3762*i
	10℃	2.9711 - 1.6413*i
	20℃	3.2455 - 1.8876*i
	30℃	3.5639 - 2.1095*i

The vertically pointing radar is configured with a zenith angle of 0°, ensuring a perfectly nadir (vertical) observation geometry. The complex refractive indices of raindrops at the X-, Ka-, and W-band frequencies at 0-30℃ used in the scattering simulations are summarized in Table 2 (Chang and Wilheit, 1979; Liebe, 1985).

To evaluate the impact of temperature on raindrop size distribution retrieval, we take DFR(Ka,W) as an example to simulate the retrieved relationship between DFR(Ka,W) and Dm for raindrops at different temperatures (Fig. 2a). As shown in Fig. 2b, the RMSE of Dm retrieval is minimized at 20°C. Therefore, the DFR–Dm retrieval model was established with 20°C adopted as the reference temperature.

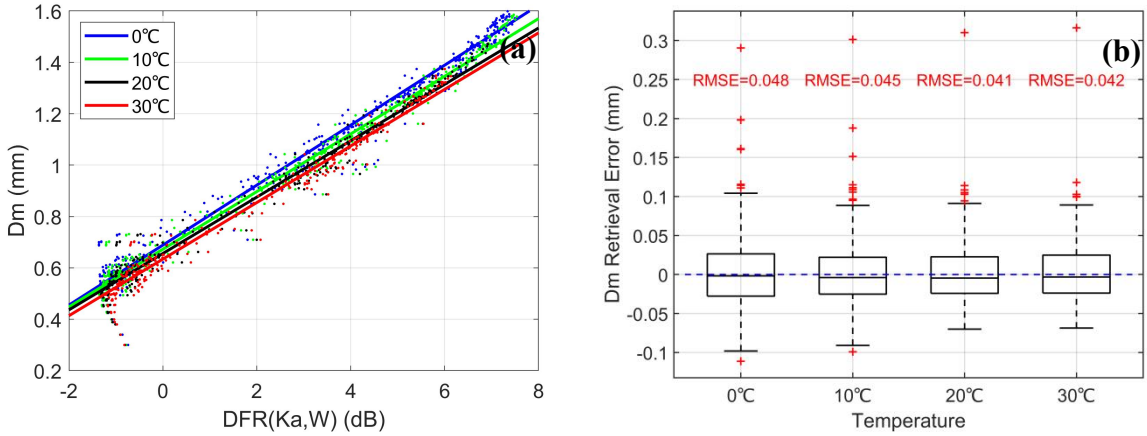

Figure 2. Fitting curves(a) and Dm retrieval error(b) of DFR(Ka,W)-Dm at different temperatures (blue: 0℃; green: 10℃; black: 20℃; red: 30℃).

3.3 Attenuation Correction

The profiles of reflectivity measured by the X/Ka dual-frequency vertically pointing radar are shown in Fig. 3. Since both X- and Ka-band signals are subject to rain-induced attenuation, attenuation correction must be applied to the observed reflectivity prior to DSD retrieval.

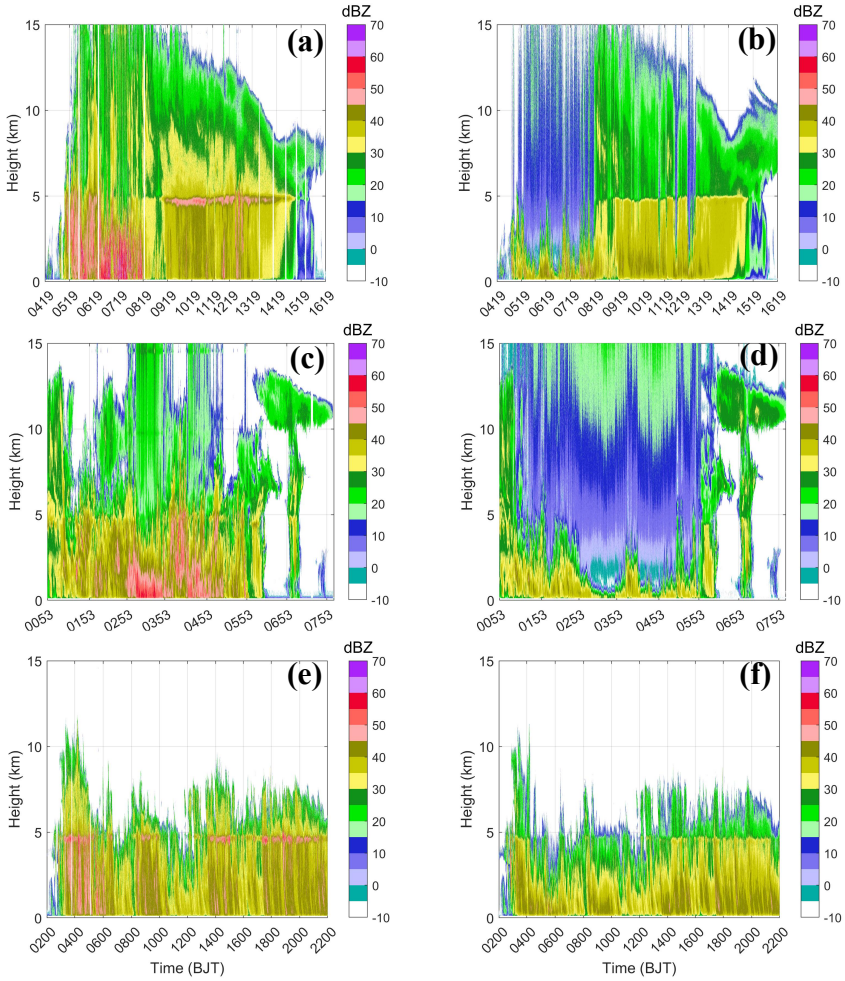

Figure 3. Time-height indicator of the dual-frequency radar reflectivity (X-band: a, c, e; Ka-band: b, d, f; top row: June 11, 2022; middle row: May 11, 2022; bottom row: May 1, 2022). The height of the melting layer bright band indicates that the zero-degree layer is approximately 5 km.

In order to ensure comprehensive coverage of various precipitation types, we utilizes observation data from May 1 and 11, 2022, June 11, 2022, and June 14, 2025. The 2022 datasets are employed to construct the raindrop size distribution retrieval model, while the observation data from June 14, 2025, serve for model validation. The case on May 1, 2022 was dominated by stratiform precipitation, while the case on May 11, 2022 was dominated by convective precipitation. The June 11, 2022 case evolved from convective to stratiform precipitation as the convective activity gradually weakened.

Taking the case on June 11, 2022 as an example, the X-band exhibits less attenuation than the Ka-band. As a result, a pronounced bright band near the melting layer is evident at X-band in the stratiform precipitation (Fig. 3a), whereas the corresponding feature is barely discernible at Ka-band (Fig. 3b). Junyent et al. (2019) found that Mie scattering at X-band becomes significant only when raindrop diameters exceed approximately 6 mm. Chudler et al. (2022) found that raindrops

exceeding 4.5 mm in diameter primarily form through the melting of hail and graupel, not the warm-rain process. As no hail or graupel was observed during either event, Mie scattering at X-band is expected to be negligible. Therefore, the X-band reflectivity is primarily influenced by rain attenuation, while Ka-band reflectivity is affected by both attenuation and Mie scattering.

Fig. 4 shows the ground-measured rain rate, Dm and Nw for the three precipitation events, including both extreme precipitation with hourly rain rate exceeding 100 mm h^{-1} (Fig. 4a: 0519-0719 BJT; Fig. 4b: 0253-0453 BJT) and stable stratiform precipitation (Fig. 4a: 0819-1019 BJT; Fig. 4c: 0800-2200 BJT).

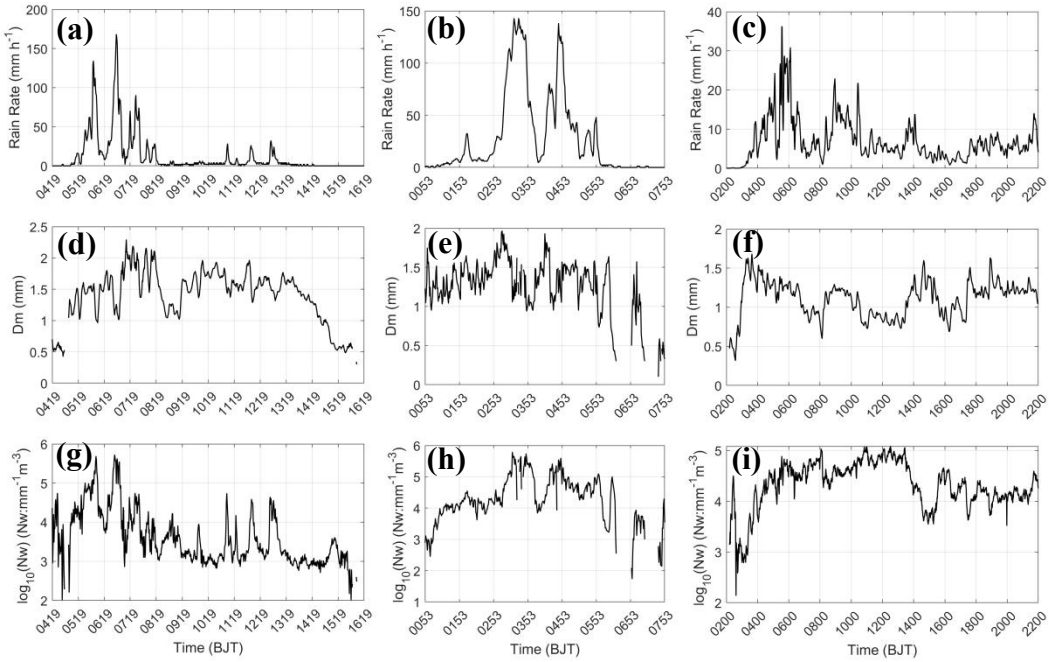

Figure 4. Time series plots of ground-observed rain rate (a-c), mass-weighted mean diameter (Dm, d-f), and normalized intercept parameter (Nw, g-i). (left: June 11, 2022; middle: May 11, 2022; right: May 1, 2022).

The X/Ka reflectivity is corrected for attenuation by applying the differential specific attenuation (Meneghini et al., 1992). The differential specific attenuation of the X/Ka-band is defined as:

$$k(X,Ka)=\frac{[Z_{X\text{-}obs}(r_2)-Z_{Ka\text{-}obs}(r_2)]-[Z_{X\text{-}obs}(r_1)-Z_{Ka}\text{-}obs(r_1)]}{2(r_2-r_1)} \tag{12}$$

where r_1, r_2 represent the near and far ends of the radar beam path, respectively. $Z_{Ka\text{-}obs}(r_1)$ and $Z_{Ka\text{-}obs}(r_2)$ denote the Ka-band observed reflectivity at the near and far ranges, while $Z_{X\text{-}obs}(r_1)$ and $Z_{X\text{-}obs}(r_2)$ denote the corresponding X-band observed reflectivity. The relationships between the specific attenuation at X-band (A_X), Ka-band (A_{Ka}), and k(X, Ka) are estimated by scattering simulation based on measured DSDs (Fig. 5).

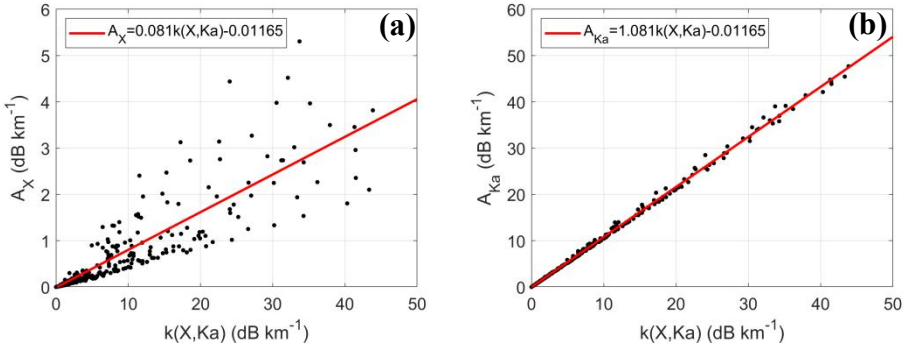

Figure 5. Scatterplots of the differential specific attenuation [k(X,Ka)] and specific attenuation (a: A_X, b: A_{Ka}).

The differential specific attenuation formula provides accurate results when hydrometeors are relatively small and Mie scattering is negligible at both X- and Ka-band. However, in the presence of larger particles where Mie scattering becomes significant at Ka-band, the differential specific attenuation tends to be overestimated, leading to inflated values of A_X and A_{Ka}. To address this, the attenuation correction procedure for X/Ka dual-frequency radar should be constrained by theoretical DFR(X, Ka) values obtained from fitted scattering simulation results.

Furthermore, to reduce the ambiguity of DFR(X, Ka)-Dm, theoretical DFR(Ka, W) are similarly obtained and used to retrieve Dm when DFR(X, Ka) is less than 0 (Section 3.5). The scattering simulation results and fitted curves are illustrated in Fig. 6, and the corresponding polynomial coefficients are listed in Table 3.

$$y=p_1x^6+p_2x^5+p_3x^4+p_4x^3+p_5x^2+p_6x+p_7 \tag{13}$$

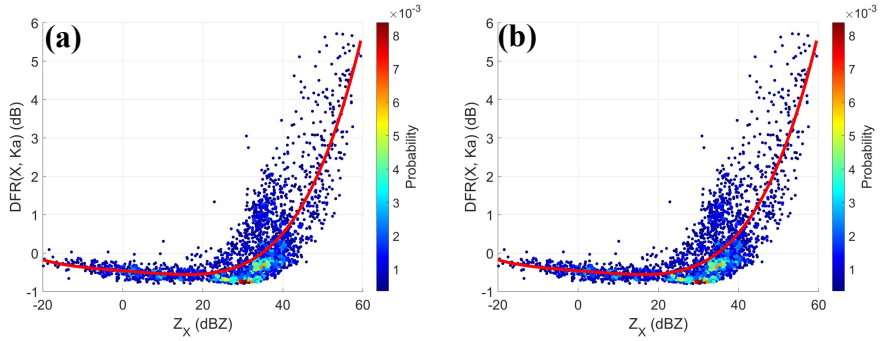

Figure 6. Scatterplots of the X-band reflectivity (Z_X) and X/Ka dual-frequency ratio [DFR(X, Ka)]; the Ka-band reflectivity (Z_{Ka}), and Ka/W dual-frequency ratio [DFR(Ka, W)]. The red curve represents the polynomial fit.

Table 3. Coefficients of the fitted polynomial

coefficients	Z_{Ka}-DFR(Ka, W)	Z_X-DFR(X, Ka)
p1	-4.823×10-10	0
p2	-8.014×10-9	0
p3	2.746×10-6	5.456×10-7

p4	-7.539×10-5	-2.216×10-6
p5	2.419×10-3	3.618×10-5
p6	8.842×10-2	-8.324×10-3
p7	-6.192×10-2	-4.585×10-1

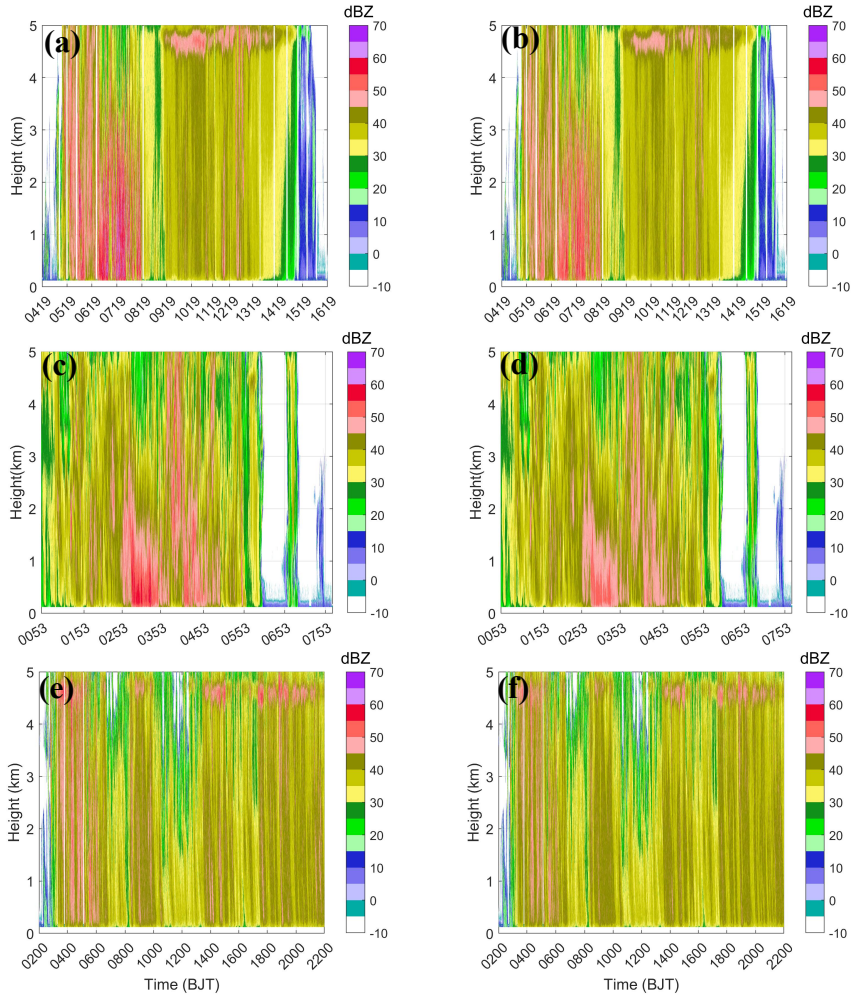

Figure 7. Corrected reflectivity of the dual-frequency radar (X-band: a, c, e; Ka-band: b, d, f; top: June 11, 2022; middle: May 11, 2022; bottom: May 1, 2022).

Since this study focuses on retrieving raindrop size distributions, all figures presented herein display physical parameters exclusively below the melting layer. As shown in Figure 7, the corrected reflectivities at X- and Ka-band exhibit improved consistency within weak echo regions. In contrast, within strong echo zones, the corrected X-band reflectivity exceeds that at Ka-band, which aligns with theoretical expectations that the dual-frequency ratio increases with reflectivity. Additionally, a

bright band feature is evident near the melting layer in the corrected Ka-band reflectivity (Fig. 7b). A similar effect was observed on 1 May 2022 (Fig. 7f), further supporting the physical consistency and accuracy of the attenuation correction.

The corrected reflectivities were validated against the theoretical reflectivity values derived from ground-based raindrop size distributions measurements. The X/Ka dual-frequency radar begins recording at the fourth gate (gate length: 30 m) and the reflectivity at 120 m is taken as an approximation of the ground-level value. As shown in Figure 8a, the X-band reflectivity exhibits negligible attenuation and closely agrees with the values calculated from raindrop size distributions. While the Ka-band reflectivity suffers marked attenuation (especially above 30 dBZ, Fig. 8b), the corrected results demonstrate close agreement with theoretical values.

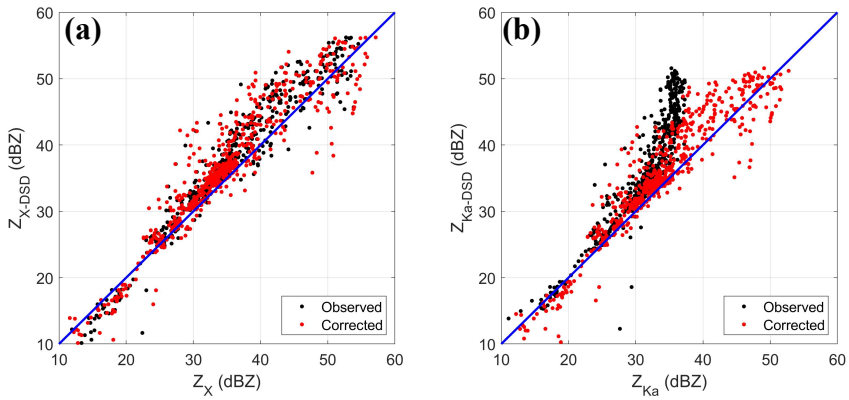

Figure 8. The comparison between the observed and corrected reflectivity values for X-band (Z_X) and Ka-band (Z_{Ka}) at 120m height and the corresponding reflectivity derived from measured raindrop size distributions ($Z_{X\text{-}DSD}$, $Z_{Ka\text{-}DSD}$).

The performance of the attenuation correction was quantitatively evaluated using the mean bias (MB), mean absolute error (MAE), root mean square error (RMSE) and correlation coefficient (CC), defined as follows:

$$MB = \frac{1}{n}\sum_{i=1}^{n}(E_i - T_i) \tag{14}$$

$$MAE = \frac{1}{n}\sum_{i=1}^{n}|E_i - T_i| \tag{15}$$

$$RMSE = \sqrt{\frac{1}{n}\sum_{i=1}^{n}(E_i - T_i)^2} \tag{16}$$

$$CC = \frac{\sum_{i=1}^{n}(E_i-\overline{E})(T_i-\overline{T})}{\sqrt{\sum_{i=1}^{n}(E_i-\overline{E})^2}\sqrt{\sum_{i=1}^{n}(T_i-\overline{T})^2}} \tag{17}$$

where E_i is the observed or corrected value, T_i is the true value, $\overline{E}$ and $\overline{T}$ is the mean value, and n is the total sample size.

As presented in Table 4, the corrected Ka-band reflectivity ($Z_{Ka\text{-}cor}$) aligns much more closely with theoretical values than the observed reflectivity ($Z_{Ka\text{-}obs}$). This improvement is evidenced by a significant reduction in MB, along with decreased MAE and RMSE, and an increased CC.

Table 4. Error statistics of Ka-band reflectivity before and after correction

Parameter	MB (dB)	MAE (dB)	RMSE (dB)	CC
$Z_{Ka\text{-}obs}$	-5.2206	5.4504	7.5531	0.9017
$Z_{Ka\text{-}cor}$	0.1720	3.0525	4.9096	0.9413

Using the accurately corrected X- and Ka-band reflectivity, the DFR(X, Ka) and DFR(Ka, W) are obtained (Fig. 9). The results show that DFR(Ka, W) has a broader dynamic range than DFR(X, Ka), and regions of high values coincide for both ratios.

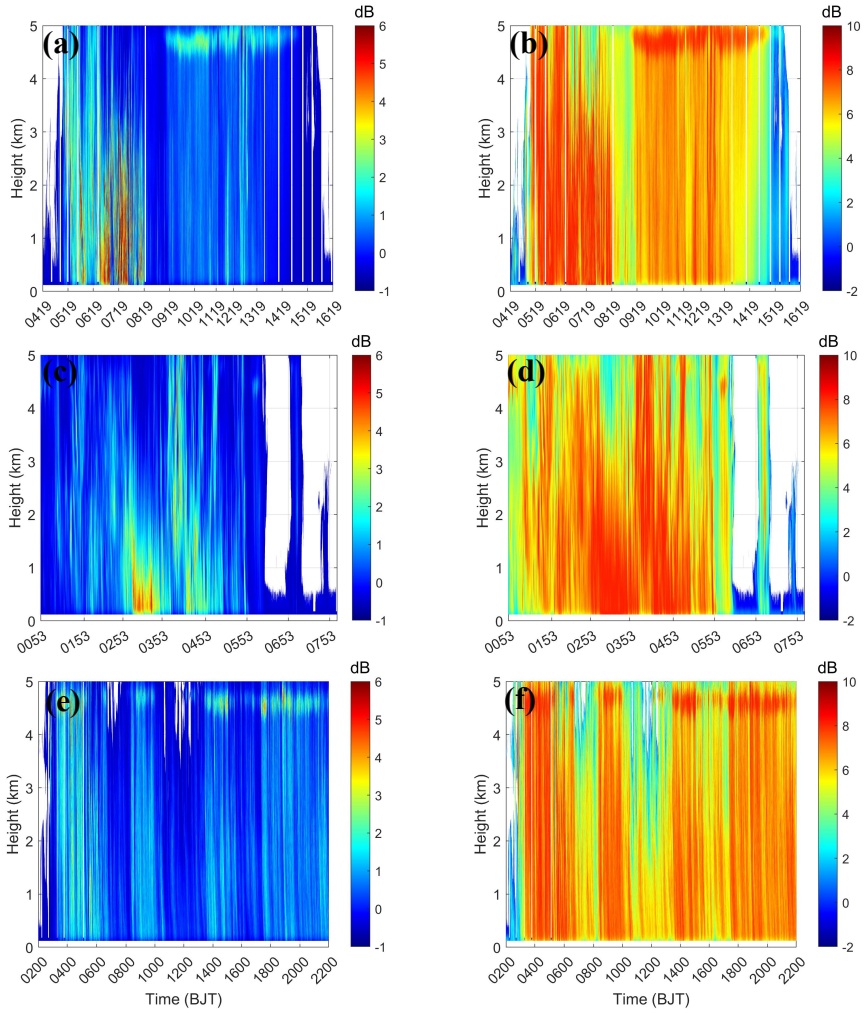

Figure 9. Time-height indicator of the dual-frequency ratio [DFR(X,Ka): a, c, e; DFR(Ka,W): b, d, f; top row: June 11, 2022; middle row: May 11, 2022; bottom row: May 1, 2022].

3.4 Sensitivity Analysis of μ

The setting of the shape parameter (μ) can influence the retrieval results. To minimize retrieval errors, the optimal value of μ was determined through sensitivity tests. As shown in Figure 10a, the retrieval error for Dm is smallest when μ = 0, and gradually increases as μ takes values of 3 and 6, though the differences among these positive values are not substantial. In contrast, Figure 10b shows that the retrieval error for Nw decreases progressively as μ increases, with μ = 3 and μ = 6 yielding notably smaller errors than μ = 0. The corresponding statistical results are summarized in Table 5.

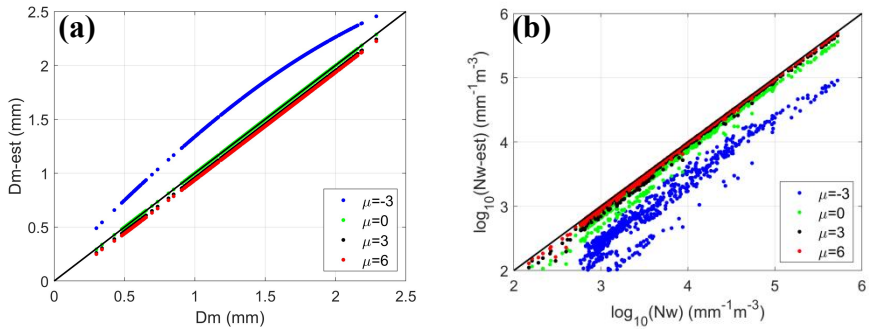

Figure 10. Sensitivity test of μ (a: retrieval of Dm; b: retrieval of Nw).

Table 5. Retrieval errors of Dm and Nw for different values of μ.

Parameter	μ	MB	MAE	RMSE
Dm	-3	0.3211	0.3211	0.3234
	0	0.0002	0.0004	0.0006
	3	-0.0466	0.0466	0.0466
	6	-0.0639	0.0639	0.0639
Nw	-3	-0.7067	0.7067	0.7414
	0	-0.1609	0.1609	0.1809
	3	-0.0684	0.0684	0.0819
	6	-0.0316	0.0316	0.0412

Although a full DSD reconstruction error metric would be desirable, the primary purpose of the retrieval framework is to estimate Dm and Nw, which are the governing parameters of the normalized gamma distribution. Therefore, Dm and Nw retrieval errors were selected as the optimization criteria in this study. To determine the optimal μ that minimizes the retrieval errors of both Dm and Nw against the ground-truth values, the Euclidean distance from each candidate μ to ideal point —serving as the cost function:

$$J=\sqrt{[\mathrm{RMSE(Dm)}-\min(\mathrm{RMSE_Dm})]^2+[\mathrm{RMSE(Nw)}-\min(\mathrm{RMSE_Nw})]^2} \tag{18}$$

Here, min(RMSE_Dm) = 0.0006 and min(RMSE_Nw) = 0.0412 (Table 5), defining the coordinates of the ideal point in the objective space. The Euclidean distance between each candidate μ and ideal point is presented in Fig. 11. The results indicate that μ=3 corresponds to the shortest distance (0.061), closely followed by μ=6 (0.063), while μ=−3 exhibits the largest deviation. Therefore, μ=3 represents the optimal value that minimizes the retrieval errors of Dm and Nw, consistent with the value adopted by Meneghini et al. (2022).

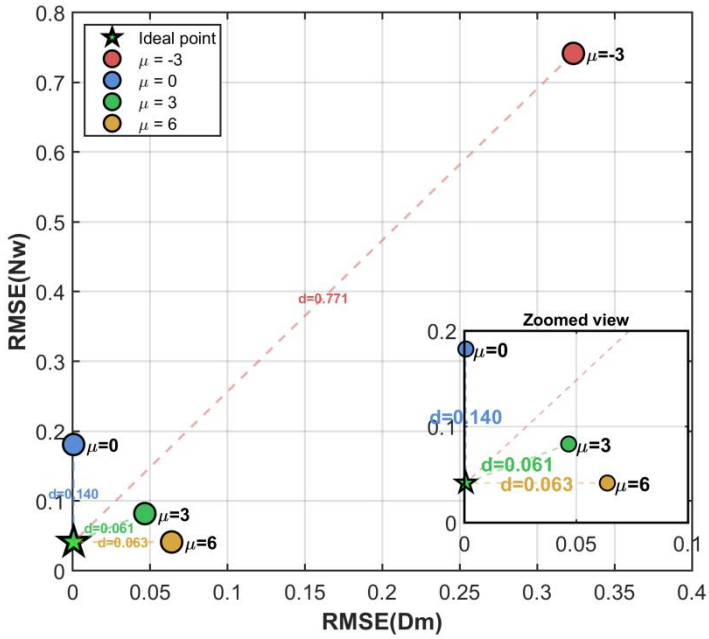

Figure 11. The Euclidean distance between each candidate μ and ideal point.

3.5 Reduction of the Ambiguous Zone in the DFR–Dm Relationship

Based on scattering simulations using the measured DSDs, the true reflectivities at X-, Ka-, and W-bands (denoted as Z_X, Z_{Ka}, and Z_W) were derived. These values were then used to compute the corresponding dual-frequency ratios [DFR(X, Ka) and DFR(Ka, W)]. As noted earlier, the relationship between DFR and Dm exhibits ambiguity when DFR is less than 0. This issue is illustrated in Fig. 12a: while a unique Dm value corresponds to each positive DFR, an ambiguous zone emerges (marked by dashed lines in Fig. 12a) for negative DFR values, where a single DFR corresponds to two different Dm values. This region is referred to as the ambiguous zone in the study.

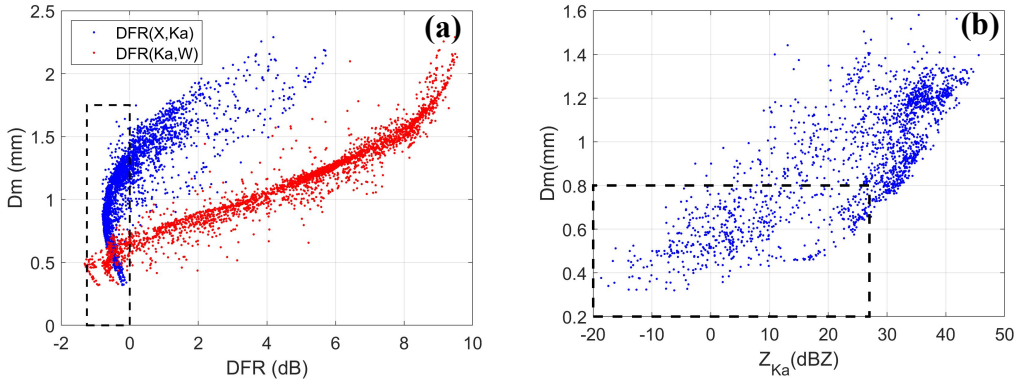

Figure 12. Scattering simulation scatterplots. (a) the DFR-Dm where blue dots represent DFR(X, Ka) and red dots represent DFR(Ka, W). The black dashed area indicates the ambiguous zone when DFR≤0. (b) the Z_{Ka}-Dm scatterplots when DFR(X, Ka)≤0, with the black dashed area representing the Z_{Ka}-Dm scatter plot when DFR(Ka, W)≤0.

Although the DFR(Ka, W)-Dm relationship also contains an ambiguous zone, its range is substantially narrower than that of DFR(X, Ka). As shown in Figure 12b, the ambiguous zone for DFR(Ka, W) is confined to a Z_{Ka} range of approximately −20 to 20 dBZ, corresponding to Dm values between 0.3 and 0.8 mm (dashed area). In comparison, the ambiguous zone for DFR(X, Ka) covers a much wider Z_{Ka} range of about −20 to 45 dBZ, corresponding to Dm values from 0.3 to 1.6 mm. Therefore, DFR(Ka, W) provides a effective constraint on Dm retrievals, particularly where DFR(X, Ka)-Dm is ambiguous. This result validates the strategy adopted in this study: using DFR(Ka, W) to resolve ambiguities in the DFR(X, Ka)-Dm relationship.

Table 6 summarizes the statistics of the DFR data used in this study. The results show that 1,013 data points fall within the unambiguous zone of DFR(X, Ka) (>0), allowing unique retrieval of Dm. In comparison, the number increases significantly to 2,505 for DFR(Ka, W) (>0), demonstrating that DFR(Ka, W) effectively narrows the ambiguity zone associated with DFR(X, Ka). Relying solely on DFR(X, Ka), only 35.38% of the dataset yields a unique Dm solution. This proportion rises markedly to 87.5% when the constraint from DFR(Ka, W) is incorporated. These results confirm that DFR(Ka, W) substantially reduces retrieval ambiguity and improves the robustness of Dm retrieval.

Table 6. Dual-frequency ratio statistical results.

DFR	DFR＞0	DFR≤0	DFR	Proportion(DFR＞0)
DFR(X,Ka)	1013	1850	2863	35.38%
DFR(Ka,W)	2505	358	2863	87.50%

4 Raindrop Size Distribution Retrieval and Evaluation

4.1 Retrieval of Dm

Given that DFR(Ka, W) exhibits a significantly narrower ambiguity zone than DFR(X, Ka), we leverage this characteristic to constrain and improve Dm retrieval. A combined approach has been formulated to resolve the ambiguity in the DFR(X, Ka)–Dm relationship. The derived relationship is presented in Fig. 13 and Eq.19.

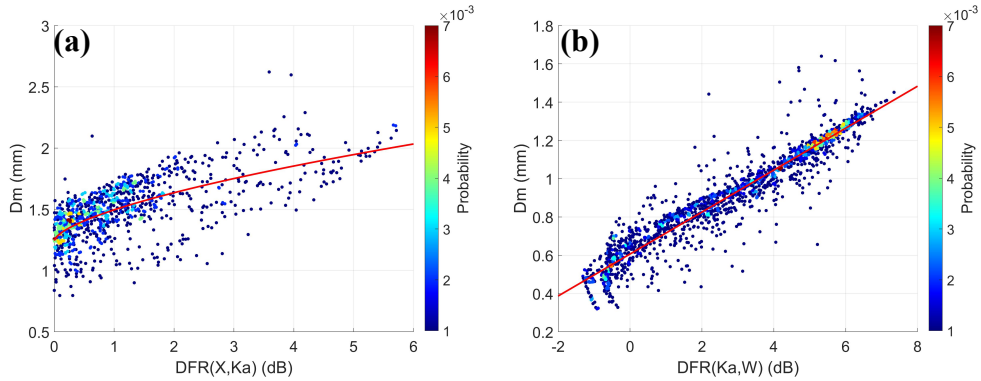

Figure 13. DFR-Dm fitting curve [a: DFR(X, Ka)>0, b: DFR(Ka, W) when DFR(X, Ka)≤0]

$$D_m=\begin{cases} 0.251\mathrm{DFR(X,Ka)}^{0.6391}+1.2445 & \mathrm{DFR(X,Ka)}>0 \\ 0.11\mathrm{DFR(Ka,W)}+0.6064 & \mathrm{DFR(X,Ka)}\leq 0 \end{cases} \tag{19}$$

As shown in Figure 13, the combination of DFR(X, Ka) and DFR(Ka, W) can accurately retrieve raindrops with Dm greater than 0.5 mm. Specifically, the DFR(Ka, W)–Dm accurately retrieves larger Dm values when DFR(Ka, W) is less than 0, with retrieval errors remaining only for raindrops smaller than 0.5 mm (Fig. 13b). Furthermore, as indicated in Fig. 14, rain rates do not exceed 0.6 mm h^{-1} when Dm is below 0.5 mm. Therefore, the retrieval error associated with DFR(Ka, W) in this range is almost negligible.

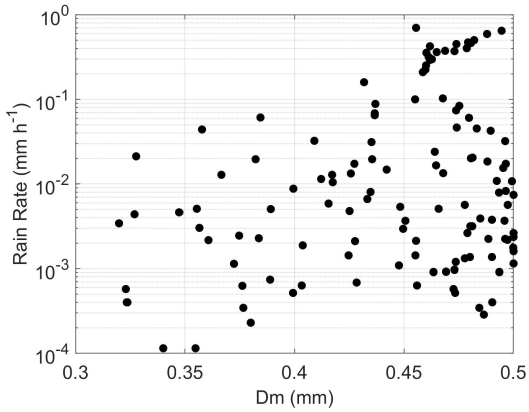

Figure 14. Scatterplots of rain rate versus Dm when Dm is below 0.5 mm based on measrued DSDs

4.2 Retrieval of Nw and LWC

The normalized intercept parameter (Nw) is retrieved by Eq. 5, which depends on both LWC and Dm. While Dm is retrieved through the combination of DFR(X, Ka) and DFR(Ka, W), the retrieval of LWC is still required. In this study, the method proposed by Oh et al. (2018) is adopted to estimate LWC from Ka-band reflectivity.

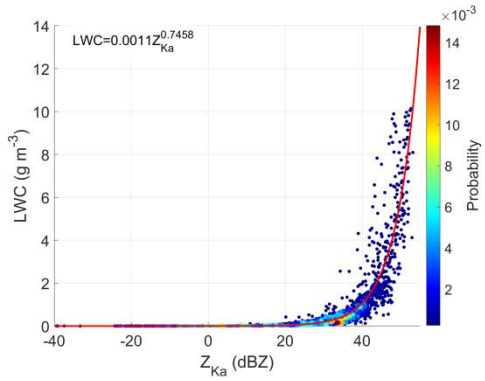

Figure 15. Scatterplots of the Ka-band reflectivity (Z_{Ka}) and liquid water content (LWC) through scattering simulation

The fitted retrieval relationship between Z_{Ka} and LWC is presented in Fig. 15. This curve is derived from T-matrix scattering simulations based on measured raindrop size distributions. The monotonic and nonlinear nature of the Z_{Ka}-LWC relationship enables reliable LWC estimation over a broad dynamic range of the reflectivity.

4.3 Retrieval Results and Validation

To investigate the vertical structure of precipitation microphysics, Figure 16 shows retrieved profiles of Dm and Nw from X/Ka-band dual-frequency radar data. The results reveal distinct microphysical characteristics between convective and stratiform precipitation. Convective clouds generally exhibit larger Dm and Nw with significant vertical inhomogeneity, whereas stratiform clouds are more uniform. Notably, Dm increases at lower altitudes accompanied by a substantial enhancement in Nw in the convective regions. This indicates the occurrence of intense microphysical processes, such as raindrop coalescence and breakup, within convective updrafts and downdrafts.

In contrast, stratiform precipitation displays vertically uniform distributions of Dm and Nw, consistent with its stable, layered structure. However, the melting layer (bright band) causes a local enhancement in these parameters, leading to peaks in Dm and Nw near the 0 °C isotherm. This characteristic is attributed to the increased radar reflectivity of melting hydrometeors.

These findings suggest that the proposed retrieval framework has the potential to capture microphysical differences across precipitation types and vertical levels, offering insights into cloud structure and precipitation formation mechanisms.

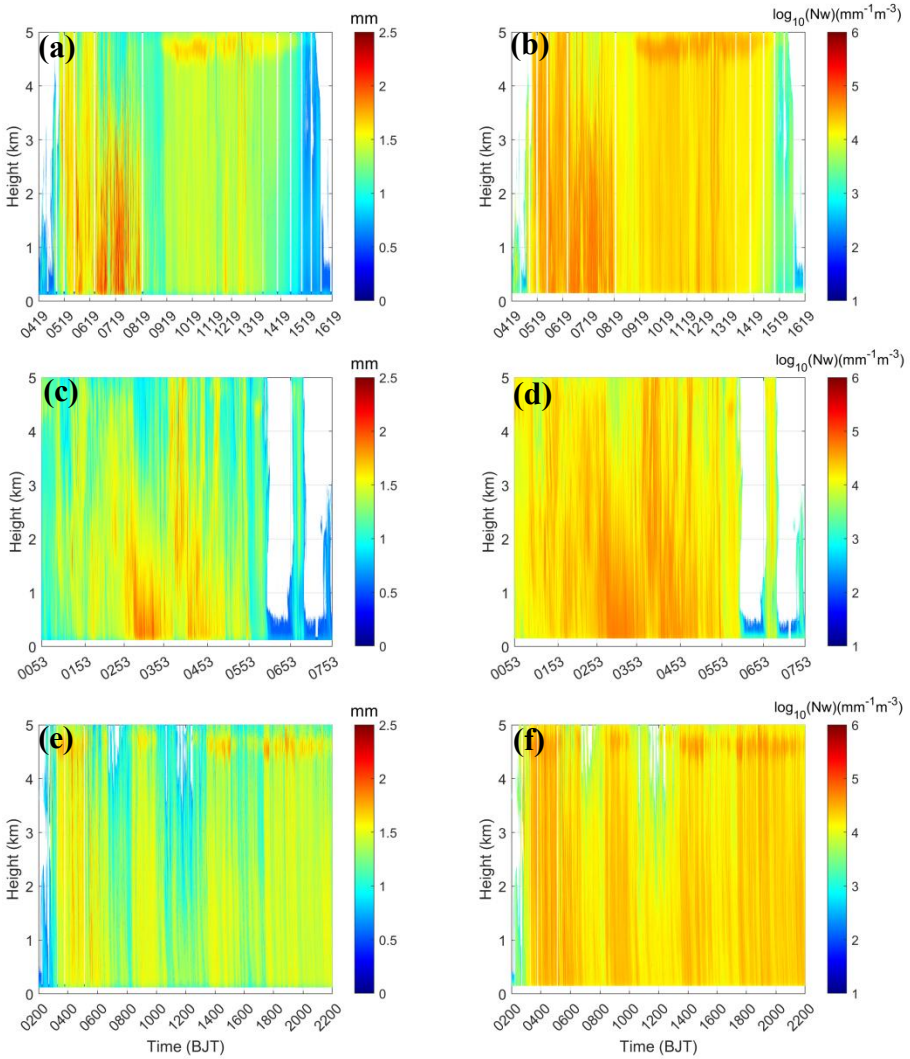

Figure 16. Time-height profiles of the mass-weighted mean diameter (Dm) and normalized intercept parameter (Nw). (Dm: a, c, e; Nw: b, d, f; top row: June 11, 2022; middle row: May 11, 2022; bottom row: May 1, 2022)

The performance of the proposed retrieval method was evaluated by comparing near-surface X/Ka-band radar retrievals with ground-based 2DVD observations. Its superiority was further demonstrated through a comparison with two conventional methods (Fig. 18) and the retrieval formula is shown in Eq. 20. The first estimates Dm only when DFR(X, Ka) > 0, ignoring the dual-solution problem (Wang et al., 2020; Liu et al., 2020). The second follows the same procedure as the first when DFR > 0, but it selects the large Dm when DFR ≤ 0 (Mardiana et al., 2004).

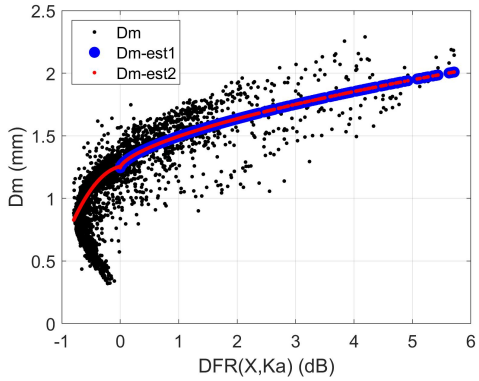

Figure 17. The mass-weighted mean diameter retrieved by conventional methods versus the true value. [Dm (black): true value; Dm-est1 (blue): the first conventional method; Dm-est2 (red): the second conventional method].

$$D_{m-est}=\begin{cases} 0.251DFR(X,Ka)^{0.6391}+1.2445 & DFR(X,Ka)>0 \\ -0.563DFR(X,Ka)^{2}+0.088DFR(X,Ka)+1.254 & DFR(X,Ka)\leq 0 \end{cases} \tag{20}$$

As shown in Figure 18, the first conventional method performs well only for large raindrops, but fails to capture Dm smaller than 1.3 mm (Fig. 18b). The second conventional method tends to overestimate the small Dm (Fig. 18c). In contrast, the proposed framework demonstrates a substantial improvement by accurately retrieving Dm across the entire size spectrum (Fig. 18a), including smaller raindrops that are commonly found in stratiform and light precipitation.

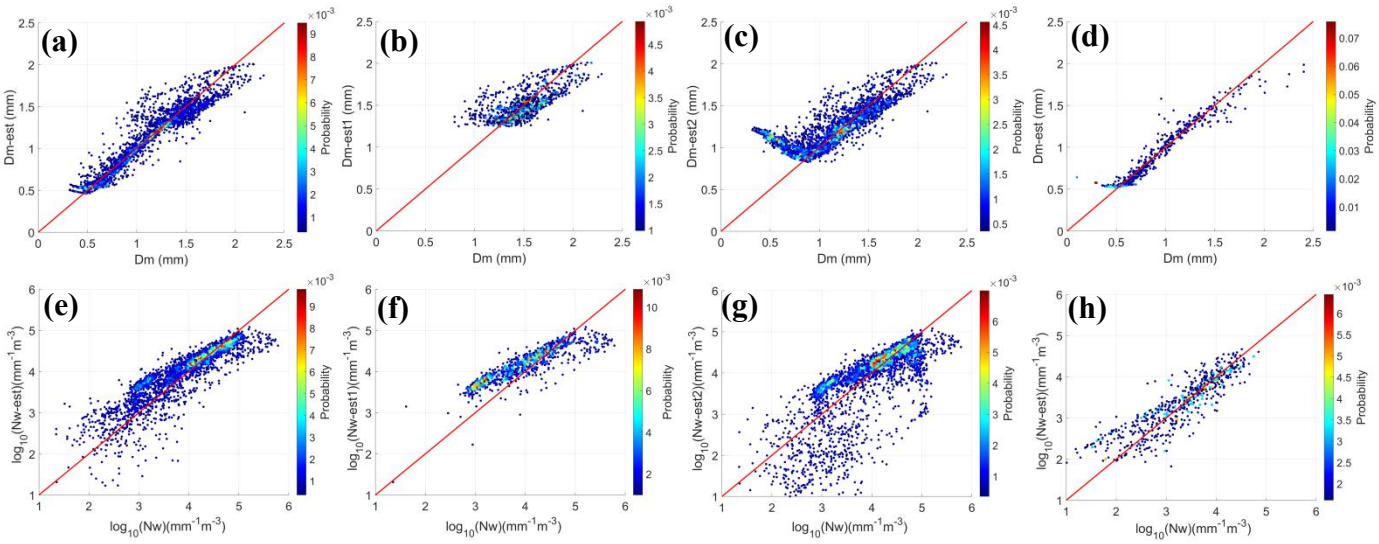

Figure18. Retrieved mass-weighted mean diameter (Dm) and normalized intercept parameter [$\log_{10}$(Nw)]. (a, e: the proposed framework; b, f: the first conventional method; c, g: the second conventional method; d, h: the retrieved Dm and Nw of June 14, 2025 by the proposed framework).

In terms of Nw retrieval, the first conventional method can only accurately retrieve Nw for large raindrops (Fig. 18f). Due to the inverse relationship between Dm and Nw, the overestimation of Dm by the second conventional method leads to underestimated Nw retrievals for small raindrops (Fig. 18g). In contrast, the proposed framework overcomes these limitations of conventional methods, demonstrating good consistency between the retrieved Nw and ground truth (Fig. 18e). Furthermore, the proposed framework was applied to a precipitation case on June 14, 2025 to evaluate its applicability. As shown in Figures 18d and 18h, the retrieval results agree well with ground-based measurements, suggesting the potential applicability of the proposed framework. As quantitatively assessed in Table 7, the proposed framework shows improved accuracy and a degree of generalizability in retrieving both Dm and Nw compared to the two conventional methods. Notably, despite the second conventional method performing better than the first for Dm retrieval, it shows weaker capability in retrieving Nw.

Table 7. Retrieval error statistics for the mass-weighted mean diameter (Dm) and the normalized intercept parameter (Nw). *Note: "-est" denotes results from the proposed framework; "-est1" and "-est2" denote results from the first and second conventional methods, respectively; "-validation" denotes the retrieval results from the proposed framework for June 14, 2025.*

Parameter	MB	MAE	RMSE	CC
Dm-est	-0.0016	0.0804	0.1242	0.9441
Dm-est1	-0.0004	0.1349	0.1491	0.6831
Dm-est2	0.0943	0.1762	0.2578	0.7829
Dm-validation	0.0321	0.0934	0.1490	0.9419
Nw-est	0.0671	0.2658	0.3662	0.8924
Nw-est1	0.1881	0.3529	0.4332	0.8761
Nw-est2	-0.1446	0.4530	0.6507	0.7504
Nw-validation	0.0676	0.2718	0.3673	0.8900

A comparison of retrieved raindrop size distributions with ground truth across reflectivity intervals is shown in Fig. 19. The proposed framework outperforms the conventional ones, accurately retrieving DSDs across all intervals with particular improvement for weak echoes (Fig. 19a). While conventional methods improve with higher reflectivity (Figs. 19b-d), the proposed framework consistently achieves the best accuracy, followed by the second and then the first conventional method. This conclusion is validated by the Dm and Nw error statistics (MB, MAE) in Fig. 20.

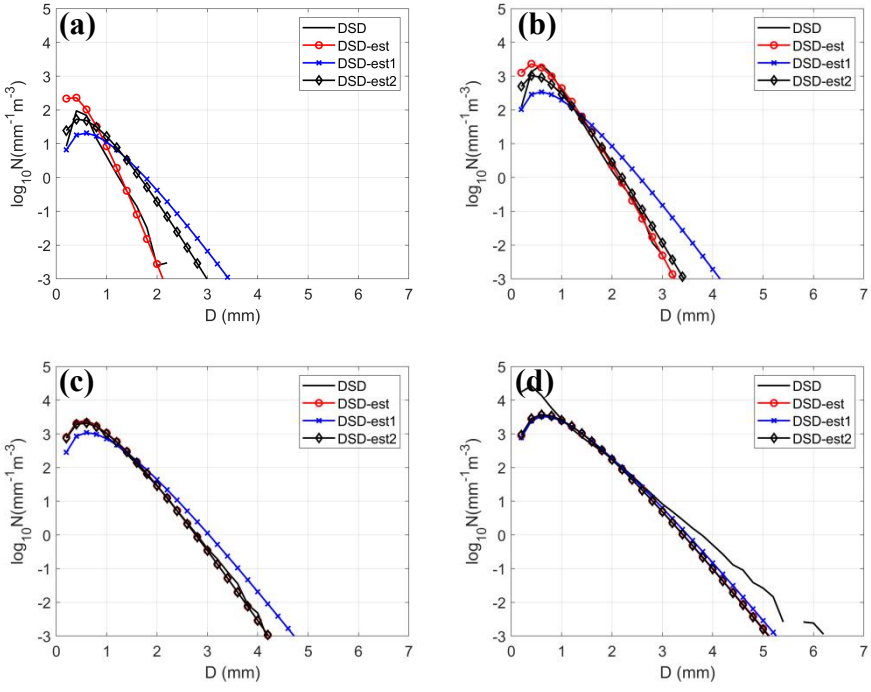

Figure 19. The mean raindrop size distributions retrieved by conventional methods (DSD-est1, DSD-est2) and the proposed framework (DSD-est) against the true values (DSD). a: Z < 20 dBZ, 655 samples; b: 20 dBZ ≤ Z < 30 dBZ, 466 samples; c: 30 dBZ≤ Z < 40 dBZ, 1281 samples; d: 40 dBZ ≤ Z < 50 dBZ, 394 samples.

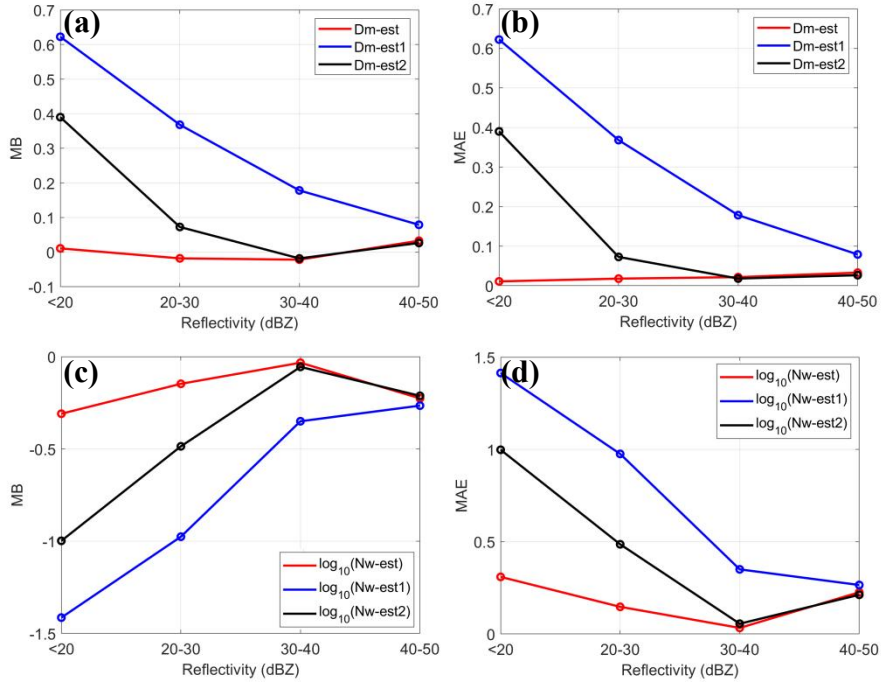

Figure 20. Retrieval performance of Dm (a, b) and $\log_{10}$(Nw) (c, d) across multiple reflectivity intervals (-est, proposed framework; -est1, first conventional method; -est2, second conventional method).

4.4 Independent Validation

The retrieval relationships (DFR-Dm and LWC-Z_{Ka}) were established using DSD data from three precipitation events in 2022 (May 1, May 11, and June 11), and the retrieval performance was independently evaluated using data from a separate precipitation event on June 14, 2025, which was not included in the relationship development.

As presented in Table 7, the independent validation results (Dm-validation and Nw-validation) demonstrate comparable accuracy to the training-period evaluation (Dm-est and Nw-est), with correlation coefficients exceeding 0.94 for Dm and 0.89 for Nw. This consistency supports the generalizability of the proposed retrieval framework to unseen precipitation events. However, it should be acknowledged that the current validation is based on a limited number of rainfall events from a single observational site and therefore may represent an upper-bound estimate of retrieval performance. Future studies will employ event-independent validation using leave-one-event-out cross-validation with a larger sample size to further quantify the robustness and generalization capability of the proposed framework.

5 Discussion and Limitations

5.1 Sensitivity of the retrieval to W-band reflectivity uncertainties

A critical question for the practical applicability of the proposed framework is the extent to which the retrieval tolerates uncertainties in the W-band reflectivity, given that no W-band radar observations are currently available and that the DFR(Ka, W) constraint is invoked in the ambiguous zone of DFR(X, Ka), where the retrieval is most vulnerable. In this section, the tolerance is quantified through a controlled sensitivity experiment.

All uncertainty sources affecting the W-band measurement act exclusively through the reflectivity itself. In logarithmic units, the calibration bias (ΔZ_{cal}) and the attenuation-correction residual (ΔZ_{att}) are additive and can be combined into a single total error term, $\delta Z_W = \Delta Z_{cal} + \Delta Z_{att}$, such that the combined reflectivity is given by $Z_W + \delta Z_W$. Since DFR(Ka, W) = dBZ(Ka) − dBZ(W), the net offset δZ_W translates into an equal and opposite shift in DFR(Ka, W). The shifted ratio is then mapped onto Dm through the fitted DFR(Ka, W)–Dm relationship (Eq. 19), and onto Nw through Nw $\propto$ Dm^{-4} (LWC being retrieved from Z_{Ka} and therefore unaffected). Consequently, a single sensitivity curve obtained by perturbing Z_W with a net offset δZ_W constitutes the complete response function of the retrieval to the combined effect of calibration errors and attenuation residuals.

The W-band reflectivities were perturbed with offsets ranging from −2 to +2 dB in steps of 0.1 dB, and the retrieval was re-run for all samples in the ambiguous zone of DFR(X, Ka). Among the ambiguous-zone samples, the fraction retaining a unique Dm solution decreases only gradually, from 80.5% at $\delta Z_W = 0$ to 72% at $|\delta Z_W| = 1$ dB (Fig. 21a). The Dm RMSE of the resolved samples increases from 0.08 mm at zero offset to 0.14 mm at $|\delta Z_W| \approx 1.1$ dB, remaining comparable to the best-

performing conventional method (0.149 mm, Table 7); beyond ±1.1 dB, the Dm RMSE exceeds that of the conventional methods, marking the point at which the advantage of the proposed framework is gradually lost (Fig. 21b). The RMSE of $\log_{10}(Nw)$ increases consistently from 0.18 to 0.33 over the same range (Fig. 21c), yet it remains lower than that obtained with the conventional method (0.433, Table 7). The results indicate that the proposed framework tolerates a combined W-band reflectivity uncertainty of approximately ±1 dB.

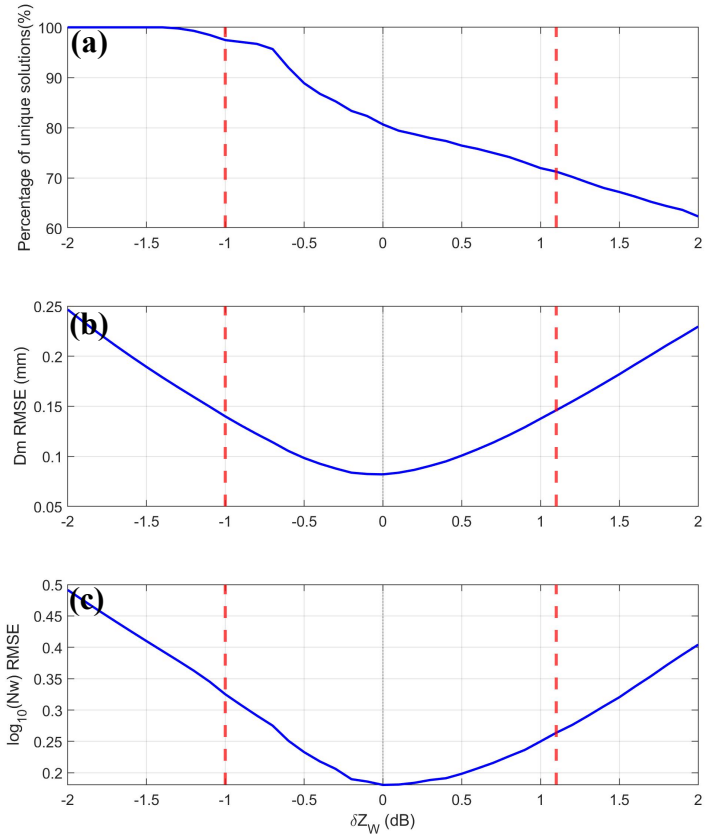

Figure 21. Sensitivity of the DSD retrieval to the combined W-band reflectivity uncertainty δZ_W, evaluated over the ambiguous-zone samples (DFR(X, Ka) ≤ 0). (a) Percentage of samples retaining a unique Dm solution, (b) Dm RMSE of the resolved samples, (c) RMSE of $\log_{10}(Nw)$. The vertical red lines in all panels indicate the threshold offsets beyond which the Dm RMSE exceeds that of the conventional methods.

5.2 Representativeness of 2DVD Validation

The validation of radar retrievals against 2DVD measurements is subject to several representativeness issues. First, wind drift during raindrop fall can cause horizontal displacement between the radar sampling volume and the disdrometer location, particularly under strong wind conditions. Second, the time required for raindrops to fall from the radar sampling height (120 m in this study) to the ground introduces a temporal lag that may result in sampling different parcels, especially for rapidly

evolving precipitation systems. Third, the fundamental difference in sampling volumes between the radar (30 meters) and the 2DVD (10 centimeters) can lead to statistical representativeness errors, particularly for inhomogeneous precipitation fields. These factors limit the accuracy and usefulness of quantitative comparisons between X/Ka dual-frequency radar and 2DVD. The 2DVD measured DSDs are used to ensure that the radar retrieved results are reasonable and relatively accurate.

5.3 Generalization and Sample Limitations

The retrieval framework presented in this study was developed and evaluated using data from a single observational site (Yangjiang, Guangdong Province) and a limited number of precipitation events (four cases total, with three used for relationship development and one for independent validation). While the cases include both stratiform and convective precipitation types, the sample size is insufficient to fully characterize the performance of the proposed framework across diverse meteorological regimes, seasonal variations, and geographical locations. The generalization capability of the retrieval relationships to other climatic regions and precipitation regimes remains to be demonstrated. Future studies should incorporate a larger and more diverse dataset, including observations from multiple sites and different seasons, to further validate and refine the proposed retrieval framework. Furthermore, the radar operates in a vertically pointing mode in this study, which largely eliminates polarimetric differences and limits the application of polarimetric parameters. Incorporating polarimetric constraints will be one of the priorities for future work.

6 Conclusions

This study presents a proof-of-concept DSD retrieval framework that explores the potential of combining X/Ka-band radar observations with simulated DFR(Ka, W) constraints to mitigate the DFR(X, Ka)-Dm ambiguity problem. The main findings are summarized as follows:

The results suggest that the DFR(Ka, W) has the potential to significantly reduce the ambiguity in the DFR(X, Ka)-Dm relationship. The proportion of data capable of yielding a unique Dm solution increased from 35.38% to 87.5% after incorporating the simulated DFR(Ka, W) constraint. This improvement could enable more accurate retrievals of Dm in weak precipitation where DFR(X, Ka) ≤ 0.

The proposed framework shows potential advantages over conventional approaches, particularly for retrieving DSDs of weak echoes (< 20 dBZ) where conventional methods exhibit substantial errors. The independent validation using a separate precipitation event demonstrates comparable retrieval accuracy, suggesting that the proposed relationships have a degree of generalizability.

It is important to emphasize the W-band reflectivities were obtained through scattering simulations rather than actual radar observations, and the evaluation is based on a limited sample from a single observational site. The results of the sensitivity experiments demonstrate that a W-band reflectivity accuracy of approximately 1 dB is required, and that such accuracy can be achieved using current ground-based W-band radar calibration practice together with standard attenuation correction. The

practical applicability of the Ka-W constraint for operational three-frequency radar systems requires further validation with real W-band observations and more extensive datasets covering diverse precipitation regimes. Future work should also address the assumptions regarding the DSD model shape parameter, incorporate height-dependent DSD models for upper-level retrievals, and quantify the impact of radar calibration and attenuation correction uncertainties on retrieval accuracy.

Code, data, or code and data availability

The dual-frequency radar data, raindrop size distribution data, and retrieval codes will be provided upon request from the corresponding author.

Author contributions

LF had the idea for the retrieval and wrote the manuscript. JY proposed improvements to the retrieval method and guided the writing of the manuscript. ZG has provided the joint observation data from dual-frequency radar and raindrop size distribution measurements. JS, YS, and HY provided valuable feedback during the development of the retrieval method and verification of the retrieval results.

Competing interests

The contact author has declared that none of the authors has any competing interests.

Disclaimer

Copernicus Publications remains neutral with regard to jurisdictional claims made in the text, published maps, institutional affiliations, or any other geographical representation in this paper. While Copernicus Publications makes every effort to include appropriate place names, the final responsibility lies with the authors. Views expressed in the text are those of the authors and do not necessarily reflect the views of the publisher.

Acknowledgements

We gratefully acknowledge the Yangjiang Meteorological Bureau of Guangdong Province for providing the essential observational data and their dedicated efforts. We also extend our sincere thanks to the developers of the T-matrix scattering code, whose work made the scattering simulations in this research possible.

Financial support

This research is supported by the Frontier Research Program of the Chinese Academy of Sciences (XDB0760402), Beijing Science and Technology Plan Project (Z251100004525005), Guangdong Basic and Applied Basic Research Foundation (2024A1515510010), China Meteorological Administration Tornado Key Laboratory (TKL202402) and Natural Science Foundation of Hebei Province (2024304015).

Review statement

The review statement will be added by Copernicus Publications listing the handling editor as well as all contributing referees according to their status anonymous or identified.

References

Chang, A. T. C. and Wilheit, T. T.: Remote sensing of atmospheric water vapor, liquid water, and wind speed at the ocean surface by passive microwave techniques from the Nimbus 5 satellite, Radio Sci., 14, 793-802, https://doi.org/10.1029/RS014i005p00793, 1979.

Chudler, K., Rutledge S. A., and Dolan, B.: Unique radar observations of large raindrops in tropical warm rain during PISTON, Mon.Wea. Rev., 150, 2719-2736, https://doi.org/10.1175/MWR-D-21-0298.1, 2022.

Ellis, S. M. and Vivekanandan, J.: Liquid water content estimates using simultaneous S and Ka band radar measurements, Radio Science., 46, 1-15, https://doi.org/10.1029/2010RS004361, 2011.

Feng, L., Xiao, H., and Luo, L.: Simulation of polarization characteristics and attenuation of dual-polarization rain-measuring radar with T-matrix methods, Chinese Journal of Computational Physics., 36, 189-202 (in Chinese), https://doi.org/ 10.19596/j.cnki.1001-246x.7826, 2019.

Hou, A. Y., Kakar, R. K., Neeck, S., and Coauthors.: The Global Precipitation Measurement Mission, Bull. Amer. Meteor. Soc., 95, 701–722, https://doi.org/10.1175/BAMS-D-13-00164.1, 2014.

Iguchi, T. and Meneghini, R.: Stability of the dual-frequency radar equations and a new method applied to the GPM's Dual-Frequency Precipitation Radar (DPR) data, IEEE Trans. Geosci. Remote Sens., 60, 5111818, https://doi.org/10.1109/TGRS.2022.3159396, 2022.

Iguchi, T., Seto, S., Meneghini, R., Yoshida, N., Awaka, J., Le, M., Chandrasekar, V., Brodzik, S., Kubota, T., and Takahashi, N.: GPM/DPR level-2 algorithm theoretical basis document, NASA ATBD, 238 pp, 2021.

Junyent, F., Chandrasekar, V., and Kennedy, P.: Resonance Scattering Detection Using the CSU–CHILL Dual-Wavelength, Dual-Polarization Radar, J. Atmos. Oceanic Technol., 36, 1177–1198, https://doi.org/10.1175/JTECH-D-18-0074.1, 2019.

Kubota, T., Seto, S., Satoh, M., Nasuno, T., Iguchi T., Masaki, T., Kwiatkowski, J. M., and Oki, R.: Cloud Assumption of Precipitation Retrieval Algorithms for the Dual-Frequency Precipitation Radar, J. Atmos. Oceanic Technol., 37, 2015–2031, https://doi.org/10.1175/JTECH-D-20-0041.1, 2020.

Ladino-Rincon, A., Nesbitt, S. W., Girolamo, L. D., Rauber, R. M., Mcfarquhar, G. M., and Lawson, R. P.: Droplet size distribution retrieval from dual-frequency precipitation radar measurement using a deep neural network, J. Atmos. Oceanic Technol., 42, 1549-1566, https://doi.org/10.1175/JTECH-D-25-0004.1, 2025.

Li, H., Ran, Z., Liu, L., Chen, Y., Bi, Y., Zhang, Y., Chen, H., and Mao J.: Research progress in profiling cloud and precipitation microphysics characteristic with ground-based multi-frequency radar, Torrential Rain and Disasters, 42, 361-371(in Chinese), https://doi.org/ 10.12406/byzh.2023-075, 2023.

Liao, L. and Meneghini, R.: Physical evaluation of GPM DPR single- and dual-wavelength algorithms, J. Atmos. Oceanic Technol., 36, 883–902, https://doi.org/10.1175/JTECH-D-18-0210.1, 2019a.

Liao, L. and Meneghini, R.: A modified dual-wavelength technique for Ku- and Ka-band radar rain retrieval, J. Appl. Meteor. Climatol. , 58, 3–18, https://doi.org/10.1109/IGARSS.2018.8517440, 2019b.

Liao, L., Meneghini, R., and Tokay, A.: Uncertainties of GPM DPR rain estimates caused by DSD parameterizations, J. Appl. Meteor. Climatol., 53, 2524–2537, https://doi.org/10.1175/JAMC-D-14-0003.1, 2014.

Liao, L. and Meneghini, R.: A study of air/space-borne dual-wavelength radar for estimates of rain profiles, Adv. Atmos. Sci., 22, 841–851, https://doi.org/10.1007/BF02918684, 2005.

Liebe, H. J.: An updated model for millimeter wave propagation in moist air, Radio Sci., 20, 1069-1089, https://doi.org/ 10.1029/RS020i005p01069, 1985.

Liu, L., Zhang,Y., and Ding, H.: Vertical air motion and raindrop size distribution size distribution retrieval using a Ka/Ku dual-wavelength cloud radar and its preliminary application, Chinese Journal of Atmospheric Sciences, 45, 1099−1113(in Chinese), doi:10.3878/j.issn.1006-9895.2104.20200, 2021.

Liu, S. and Wang G.: Study on the impacts of DSD parameters on precipitation estimation using dual-frequency radar, Plateau Meteorology, 39, 570-580(in Chinese), https://doi.org/10.7522/j.issn.1000-0534.2019.00092, 2020.

Mardiana, R., Iguchi, T., and Takahashi, N.: A dual-frequency rain profiling method without the use of a surface reference technique, IEEE Trans. Geosci. Remote Sens., 42, 2214–2225, https://doi.org/10.1109/TGRS.2004.834647, 2004.

Marshall, J. S. and Palmer, W. M.: The distribution of raindrops with size, J. Meteor., 5, 165-166, https://doi.org/10.1175 /1520-0469(1948)005<0165:TDORWS>2.0.CO;2, 1948.

Meneghini, R., Liao, L., and Iguchi, T.: A Generalized Dual-Frequency Ratio (DFR) Approach for Rain Retrievals, J. Atmos. Oceanic Technol., 39, 1309–1329, https://doi.org/10.1175/JTECH-D-22-0002.1, 2022.

Meneghini, R., Kozu, T., Kumagai, H., and Boncyk, W. C.: A study of rain estimation methods from space using dual-wavelength radar measurements at near-nadir incidence over ocean, J. Atmos. Oceanic Technol., 9, 364–382, https://doi.org/ 10.1175/1520-0426(1992)009<0364:ASOREM>2.0.CO;2, 1992.

Meneghini, R., Kumagai, H., Wang, J. R., Iguchi, T., and Kozu, T.: Microphysical retrievals over stratiform rain using measurements from an airborne dual-wavelength radar-radiometer, IEEE Trans. Geosci. Remote Sens., 35, 487–506, https://doi.org/10.1109/36.581956, 1997.

Oh, S. B., Lee, Y. H., Jeong, J. H., Kim, Y. H., and Joo, S.: Estimation of the liquid water content and Z–LWC relation using Ka-band cloud radar and a microwave radiometer, Meteorol. Appl., 25, 423–434, https://doi.org/10.1002/met.1710, 2018.

Rose, C. R. and Chandrasekar, V.: A system approach to GPM dual-frequency retrieval. IEEE Trans. Geosci. Remote Sens., 43, 1816–1826, https://doi.org/10.1109/TGRS.2005.851165, 2005.

Seto, S., Iguchi, T., Meneghini, R., Awaka, J., Kubota, T., Masaki, T., and Takahashi, N.: The precipitation rate retrieval algorithms for the GPM Dual-Frequency Precipitation Radar, J. Meteor. Soc. Japan., 99, 205–237, https://doi.org/10.2151/jmsj.2021-011, 2021.

Seto, S., Iguchi, T., and Oki, T.: The basic performance of a precipitation retrieval algorithm for the Global Precipitation Measurement mission's single/dual-frequency radar measurements, IEEE Trans. Geosci. Remote Sens., 51, 5239–5251, https://doi.org/10.1109/TGRS.2012.2231686, 2013.

Skofronick-Jackson, G. and Coauthors.: The Global Precipitation Measurement (GPM) mission for science and society, Bull. Amer. Meteor. Soc., 98, 1679–1695, https://doi.org/10.1175/BAMS-D-15-00306.1, 2017.

Skofronick-Jackson, G., Kirschbaum, D., Petersen, W., Huffman, G., Kidd, C., Stocker, E. and Kakar, R.: The Global Precipitation Measurement (GPM) mission's scientific achievements and societal contributions: Reviewing four years of advanced rain and snow observations, Quart.J.Roy.Meteor.Soc., 144,27–48, https://doi.org/10.1002/qj.3313, 2018.

Tang, Q., Xiao, H., Guo, C., and Feng, L.: Characteristis of the raindrop size distributions and their retrieved polarimetric radar parameters in northern and southern China, Atmos. Res., 135-136, 59-75, https://doi.org/10.1016/j.atmosres.2013.08.003, 2014.

Testud, J., Oury, S., Amayenc, P., and Black, R. A.: The concept of "normalized" distributions to describe raindrop spectra: A tool for cloud physics and cloud remote sensing, J. Appl. Meteor., 40, 1118–1140, https://doi.org/10.1016/S 1464-1909(00)00122-2, 2001.

Tokay, A. and Beard, K. V.: A Field Study of Raindrop oscillations. Part I: Observation of Size Spectra and Evaluation of Oscillation Causes, J. Appl. Meteor., 35, 1671-1687, https://doi.org/10.1175/1520-0450(1996)035<1671:AFSORO>2.0.CO;2, 1996.

Ulbrich, C. W.: Natural variations in the analytical form of the raindrop size distribution, J. Climate Appl. Meteor., 22, 1764–1775, https://doi.org/10.1175/1520-0450(1983)022<1764:NVITAF>2.0.CO;2, 1983.

Wang, G., Liu, S., and Liu, L.: Uncertainties in retrieving microphysical properties of rain profiles using ground-based dual-frequency radar, Meteorol. Appl., 27, e1876, https://doi.org/10.1002/met.1876, 2020.

Waterman, P. C.: Matrix formulation of electromagnetic scattering, Proc. IEEE., 53, 805-812, https://doi.org/ 10.1109/ PROC.1965.4058, 1965.

610 Waterman, P. C.: Symmetry, unitarity and geometry in electromagnetic scattering, Phys. Rev., 3, 825-839, https://doi.org/10.1103/PhysRevD.3.825, 1971.